

# Tuning-free Plug-and-Play Hyperspectral Image Deconvolution with Deep Priors

Xiuheng Wang, *Graduate Student Member, IEEE*, Jie Chen, *Senior Member, IEEE*,  
and Cédric Richard, *Senior Member, IEEE*.

**Abstract**—Deconvolution is a widely used strategy to mitigate the blurring and noisy degradation of hyperspectral images (HSI) generated by the acquisition devices. This issue is usually addressed by solving an ill-posed inverse problem. While investigating proper image priors can enhance the deconvolution performance, it is not trivial to handcraft a powerful regularizer and to set the regularization parameters. To address these issues, in this paper we introduce a tuning-free Plug-and-Play (PnP) algorithm for HSI deconvolution. Specifically, we use the alternating direction method of multipliers (ADMM) to decompose the optimization problem into two iterative sub-problems. A flexible blind 3D denoising network (B3DDN) is designed to learn deep priors and to solve the denoising sub-problem with different noise levels. A measure of 3D residual whiteness is then investigated to adjust the penalty parameters when solving the quadratic sub-problems, as well as a stopping criterion. Experimental results on both simulated and real-world data with ground-truth demonstrate the superiority of the proposed method.

**Index Terms**—HSI deconvolution, Plug-and-Play, tuning-free, deep learning, residual whiteness, parameter estimation.

## I. INTRODUCTION

Hyperspectral imaging systems simultaneously capture images of a scene over continuous narrow spectral bands ranging from ultraviolet to visible and infrared. The high spectral resolution provided by HSIs enables us to conduct analyses that cannot be performed with conventional imaging techniques. Benefiting from abundant spectral information, hyperspectral imaging has been widely applied to applications as diverse as remote sensing [2] and computer vision [3]. However, due to various physical and hardware limitations, observed HSIs are usually blurred and corrupted by noise during the acquisition process, leading to degraded performance in subsequent analyses. Thus, it is desirable to restore images by deconvolution (inversion of the degradation process) techniques beforehand.

Multichannel images contain abundant spectral information across neighboring wavelengths, which raises the challenge of accounting for spectral correlations while ensuring spatial consistency compared to ordinary 2D images [4], [5]. State-of-the-art deconvolution of multichannel (multispectral) images involves Wiener filter [6], [7], Kalman filter [8], and regularized least-squares [9]. For hyperspectral deconvolution,

A preliminary version of this work has been published in the proceedings of the 2020 IEEE International Conference on Acoustics, Speech and Signal Processing (ICASSP) [1]. Xiuheng Wang and Cédric Richard are with Université Côte d’Azur, CNRS, OCA, F-06108, Nice, France (e-mail: xiuheng.wang@oca.eu, cedric.richard@unice.fr). Jie Chen is with Centre of Intelligent Acoustics and Immersive Communications at School of Marine Science and Technology, Northwestern Polytechnical University, Xi’an, 710072, China (e-mail: dr.jie.chen@ieee.org).

an adaptive 3D Wiener filter [10] and a filter-based linear method [4] have been used for astronomic HSIs. 2D Fast Fourier Transforms (FFTs) and Fourier-wavelet techniques have been considered in [11] and [12] for HSI deconvolution in order to benefit from computational efficiency in Fourier and wavelet domains. In [13], an online deconvolution algorithm was devised to process HSIs sequentially collected by a push-broom device.

Considering that deconvolution problems are usually highly ill-posed, it is strongly desirable to incorporate prior information of images to regularize the solutions. To this end, a computationally-efficient algorithm in [14] performs HSI deconvolution subject to positivity constraints while accounting for spatial and spectral correlations. The work in [15] investigates both the spatial non-local self-similarity and spectral correlations by employing low-rank tensor priors. Defining proper priors and designing regularizers play a key role with these methods. However it is not a trivial task to handcraft powerful regularizers, having in mind that complex regularizers may also introduce extra difficulties in solving optimization problems. Recently, benefiting from the variable splitting principle, various PnP methods have been proposed recently. They consist of plugging image denoising modules in optimization modules to solve inverse problems. We shall now outline the main principles of the PnP framework.

Consider the general inverse problem consisting of minimizing the following objective function:

$$\hat{\mathbf{x}} = \arg \min_{\mathbf{x}} \mathcal{D}(\mathbf{x}) + \lambda \mathcal{R}(\mathbf{x}), \quad (1)$$

where  $\mathbf{x}$  is the unknown variable to be estimated,  $\mathcal{D}(\mathbf{x})$  is the data fidelity term that ensures the consistency between the reconstructed and observed signals, and  $\mathcal{R}(\mathbf{x})$  is a regularizer that enforces desirable properties of the solution with  $\lambda \geq 0$  the regularization parameter. With the ADMM [16] or the half quadratic splitting method [17], the optimization problem (1) can be solved in  $K$  iterations consisting of two key operations:

$$\hat{\mathbf{x}} = \arg \min_{\mathbf{x}} \mathcal{D}(\mathbf{x}) + \frac{\rho}{2} \|\mathbf{x} - \hat{\mathbf{v}}\|_2^2; \quad (2)$$

$$\hat{\mathbf{v}} = \text{Denoiser}(\hat{\mathbf{x}}, \sigma); \quad (3)$$

where  $\rho$  is the penalty parameter, and  $\text{Denoiser}(\cdot)$  represents a denoising operator with  $\sigma = \sqrt{\lambda/\rho}$  the denoising strength. Conversely, this formulation can also implicitly define  $\mathcal{R}(\cdot)$  when plugging an arbitrary denoising operator. This allows to benefit from the merits of deep learning and optimization methods [18], and to eliminate the need for expensive net-

work retraining whenever the inverse problem changes [19]. Applications include magnetic resonance imaging (MRI) reconstruction [19], [20], 2D image restoration [21]–[24] and hyperspectral unmixing [25], [26]. Despite its effectiveness, this strategy has not yet been employed in HSI deconvolution problems, though similar difficulties of designing regularizers are encountered there.

Regardless of whether the regularizers are manually designed or implicitly learned as in recent PnP algorithms, it is desirable to select the regularization parameters properly to balance the contribution of prior information and observations. Classic parameter estimation methods used with handcrafted regularizers include the discrepancy principle (DP) [27], the L-curve [28], [29], the generalized cross-validation (GCV) [30], [31], and Stein’s unbiased risk estimate (SURE) [32], [33]. Recently, the authors of [34] proposed the maximum curvature criterion and the minimum distance criterion (MDC) on the response surface to estimate the regularization parameters in a non-negative HSI deconvolution problem [14]. The MDC has been extended to HSI super-resolution by considering a deep prior regularizer in [35]. By defining and maximizing some whiteness measures of residual images, the authors of [36] proposed a 2D image deblurring method with objective criteria for adjusting the regularization parameter as well as the stopping criterion. In [37], an exact residual whiteness principle has been proposed for generalized Tikhonov-regularized 2D image restoration. However, a specific-designed criteria for 3D images, such as HSIs, is still missing.

Compared to handcrafted regularizers, implicit regularizers in PnP algorithms introduces extra challenges that need to be addressed for devising an automatic regularization parameter estimation strategy. In the PnP framework,  $\lambda$  is reparameterized by a series of internal parameters, including the penalty parameter  $\rho$ , the denoising strength  $\sigma$ , and the number of iterations  $K$  (related to stopping criteria). In [21], [25], [26], a constant scaling factor is used to increase  $\rho$  linearly as iterations proceed. In [22],  $\sigma$  is exponentially decayed in sequential denoising sub-problems. Nevertheless, the selected parameters in all these handcrafted criteria may lead to sub-optimal performance since the internal parameters may not change monotonically. To address this issue, the methods in [23], [24] consist of training a blind denoising network to estimate  $\sigma$  automatically. The work in [23] considers a fixed  $\rho$  while the approach in [24] considers a fixed  $\lambda$ . Unlike these semi-automated approaches, deep reinforcement learning is used in [19] to determine all the internal parameters, leading to good convergence behavior and performance.

In this paper, we introduce a fully automatic PnP hyperspectral deconvolution method that uses spectral-spatial priors learned from data by a deep neural network. The HSI deconvolution problem is addressed with an ADMM algorithm. In order to avoid manually selecting the regularization parameters, we define a non-negative scalar measure of whiteness for 3D residual images, which cooperates with a blind deep denoiser to adaptively adjust all the internal parameters. The contributions of this work are summarized as follows:

- We propose a PnP framework for hyperspectral deconvolution. Based on the ADMM algorithm, the optimization

problem is split into two sub-problems, a simple quadratic sub-problem and a 3D-image denoising sub-problem.

- A blind deep denoiser B3DDN is designed and plugged into the proposed framework. This denoising operator learns both spatial context and spectral attributes of HSIs, bypassing the difficulty in designing regularizers. After training with simulated data, the flexibility of the B3DDN allows it to learn, without any extra training, the priors for real-world images even with a distinct number of spectral channels.
- The proposed PnP framework is designed in a completely turning-free manner. Specifically, the penalty parameters are determined automatically by solving a scalar optimization problem while the denoising strengths are implicitly learned by the B3DDN. A stopping criterion for the iterative process is also provided.
- An HSI dataset containing six blurring and clear image pairs captured in indoor and outdoor scenes is provided with this work. This dataset allows us to show that our method is applicable with real-world scenarios. It also provides a benchmark for future research works in hyperspectral deconvolution.

The paper is organized as follows. In Section II, HSI deconvolution is formulated as a linear inverse problem. Section III introduces the proposed tuning-free deconvolution method based on the PnP framework with learned deep priors. In Section IV, experiments with simulated and real-world data are conducted and analyzed. Section V concludes this paper.

## II. PROBLEM FORMULATION

We denote a degraded HSI and its latent clean counterpart by  $\mathbf{Y} \in \mathbb{R}^{N \times P \times Q}$  and  $\mathbf{X} \in \mathbb{R}^{N \times P \times Q}$  respectively, where  $P$ ,  $Q$ , and  $N$  are the numbers of rows, columns and spectral bands of the image. Using lexicographical order,  $\mathbf{Y}$  and  $\mathbf{X}$  can be reshaped into vectors  $\mathbf{y} \in \mathbb{R}^{NPQ \times 1}$  and  $\mathbf{x} \in \mathbb{R}^{NPQ \times 1}$ , respectively. The degraded image and the clean image at the  $i$ -th spectral band are denoted by  $\mathbf{Y}_i \in \mathbb{R}^{P \times Q}$  and  $\mathbf{X}_i \in \mathbb{R}^{P \times Q}$ . For ease of mathematical formulation, the columns of  $\mathbf{Y}_i$  and  $\mathbf{X}_i$  are stacked to form vectors  $\mathbf{y}_i \in \mathbb{R}^{PQ \times 1}$  and  $\mathbf{x}_i \in \mathbb{R}^{PQ \times 1}$ .  $\mathbf{x}$  and  $\mathbf{y}$  are vectors obtained by stacking vectors  $\mathbf{x}_i$  and  $\mathbf{y}_i$  ( $1 \leq i \leq N$ ), respectively. This notation system also works for other images.

For the  $i$ -th channel,  $\mathbf{Y}_i$  is generated from  $\mathbf{X}_i$  according to the following 2D degradation model:

$$\mathbf{Y}_i = \mathcal{H}_i * \mathbf{X}_i + \mathbf{N}_i \quad (4)$$

where  $\mathcal{H}_i$  is the convolution kernel, possibly containing null entries, of size  $P \times Q$  encoding the Point Spread Function (PSF) of the  $i$ -th channel:

$$\mathcal{H}_i = \begin{pmatrix} \mathcal{H}_{11} & \cdots & \mathcal{H}_{1Q} \\ \vdots & \ddots & \vdots \\ \mathcal{H}_{P1} & \cdots & \mathcal{H}_{PQ} \end{pmatrix}, \quad (5)$$

Operator  $*$  denotes the discrete 2D convolution performed in the image domain, and  $\mathbf{N}_i$  is an additive independent and identically distributed (i.i.d.) Gaussian noise with standard

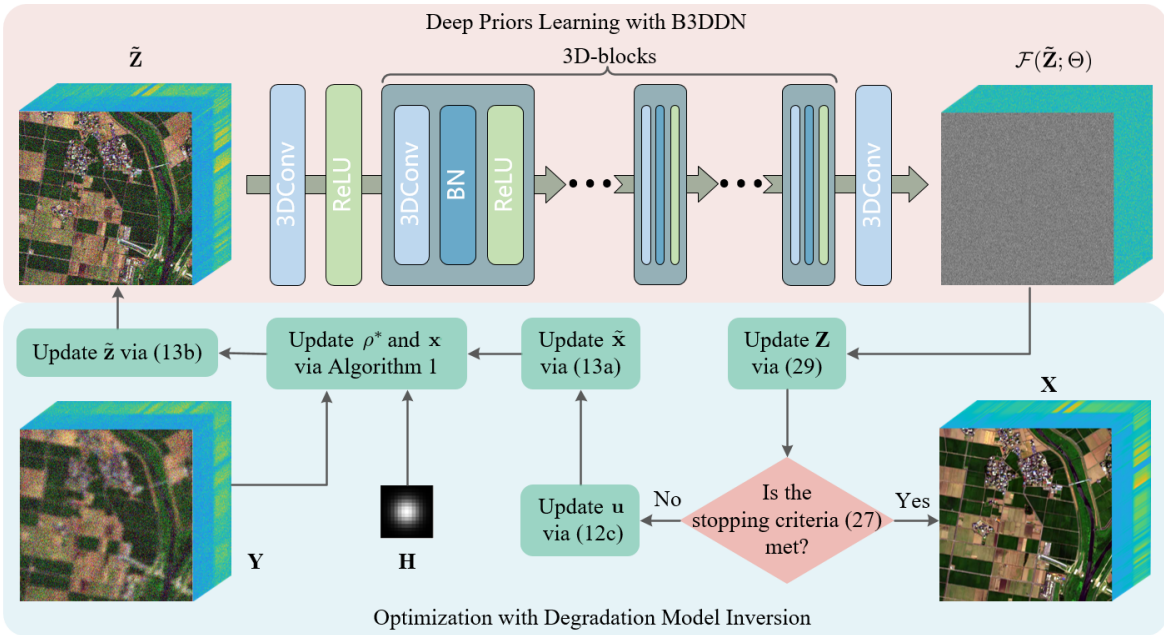


Fig. 1. Architecture of the proposed tuning-free scheme for hyperspectral image deconvolution. (top) Network structure of the B3DDN. (bottom) Numerical optimization steps in the ADMM framework.

deviation  $\sigma$ . Following [14], model (5) can be written as:

$$\mathbf{y}_i = \mathbf{H}_i \mathbf{x}_i + \mathbf{n}_i \quad (6)$$

where  $\mathbf{H}_i$  is a  $PQ \times PQ$  block-Toeplitz matrix with  $P \times Q$  Toeplitz blocks. Imposing periodic boundary conditions on  $\mathcal{H}_i$ ,  $\mathbf{H}_i$  can be rewritten as a block circulant matrix with circulant blocks, a structure denoted as circulant-block-circulant (CBC). This property allows us to design a Fourier domain implementation for solving the least square problem in Section III-A.

Assuming that the convolution is separable and the noise variance is independent over spectral bands, the hyperspectral degradation model can be written as:

$$\mathbf{y} = \mathbf{H}\mathbf{x} + \mathbf{n} \quad (7)$$

where  $\mathbf{H}$  is a block-diagonal matrix of size  $NPQ \times NPQ$ :

$$\mathbf{H} = \begin{bmatrix} \mathbf{H}_1 & \mathbf{0} & \cdots & \mathbf{0} \\ \mathbf{0} & \ddots & \ddots & \vdots \\ \vdots & \ddots & \ddots & \mathbf{0} \\ \mathbf{0} & \cdots & \mathbf{0} & \mathbf{H}_N \end{bmatrix}. \quad (8)$$

The problem in HSI deconvolution is formulated as an inverse problem, where  $\mathbf{x}$  is estimated by seeking the minimum of the following objective function:

$$\hat{\mathbf{x}} = \arg \min_{\mathbf{x}} \frac{1}{2} \|\mathbf{y} - \mathbf{H}\mathbf{x}\|^2 + \lambda \Phi(\mathbf{x}) \quad (9)$$

where the first squared-error term  $\frac{1}{2} \|\mathbf{y} - \mathbf{H}\mathbf{x}\|^2$  is the data fidelity term, and  $\Phi(\mathbf{x})$  is the regularizer.

### III. PROPOSED METHOD

Designing an effective regularizer  $\Phi(\mathbf{x})$  along with an efficient solving method is not trivial. Meanwhile, it is cumbersome to fine-tune the hyperparameter  $\lambda$  to balance the

contribution of  $\Phi(\mathbf{x})$  for different images. To tackle these issues, we propose to learn priors from hyperspectral data and incorporate it into the model-based optimization to tackle the regularized inverse problem in (9). More specifically, using the variable splitting technique, we transform problem (9) into two sub-problems, namely, a simple quadratic problem with a penalty parameter and a 3D-image denoising problem with a certain denoising strength. These sub-problems are iteratively solved, using a linear method and a blind deep neural network, respectively, until the convergence criterion is met. In this procedure, the penalty parameter is automatically estimated while the denoising strength is implicitly learned. Finally, the algorithm is automatically terminated by stopping criteria. Our tuning-free HSI deconvolution scheme is illustrated in Fig. 1.

#### A. Variable splitting based on the ADMM

The ADMM is adopted to decouple the data fidelity term and the regularization term in (9). By introducing an auxiliary variable  $\mathbf{z}$ , problem (9) can be written in the equivalent form:

$$\hat{\mathbf{x}} = \arg \min_{\mathbf{x}} \frac{1}{2} \|\mathbf{y} - \mathbf{H}\mathbf{x}\|^2 + \lambda \Phi(\mathbf{z}), \quad \text{s.t. } \mathbf{z} = \mathbf{x}. \quad (10)$$

The associated augmented Lagrangian function is given by

$$\mathcal{L}_\rho(\mathbf{x}, \mathbf{z}, \mathbf{v}) = \arg \min_{\mathbf{x}} \frac{1}{2} \|\mathbf{y} - \mathbf{H}\mathbf{x}\|^2 + \lambda \Phi(\mathbf{z}) + \mathbf{v}^T (\mathbf{x} - \mathbf{z}) + \frac{\rho}{2} \|\mathbf{x} - \mathbf{z}\|^2 \quad (11)$$

with  $\mathbf{v}$  the dual variable, and  $\rho > 0$  the penalty parameter. Scaling  $\mathbf{v}$  as  $\mathbf{u} = \frac{1}{\rho} \mathbf{v}$ , problem (11) can be iteratively solved

by repeating the following successive steps:

$$\mathbf{x}_{k+1} = \arg \min_{\mathbf{x}} \frac{1}{2} \|\mathbf{y} - \mathbf{H}\mathbf{x}\|^2 + \frac{\rho_k}{2} \|\mathbf{x} - \tilde{\mathbf{x}}_k\|^2 \quad (12a)$$

$$\mathbf{z}_{k+1} = \arg \min_{\mathbf{z}} \lambda \Phi(\mathbf{z}) + \frac{\rho_k}{2} \|\tilde{\mathbf{z}}_k - \mathbf{z}\|^2 \quad (12b)$$

$$\mathbf{u}_{k+1} = \mathbf{u}_k + \mathbf{x}_{k+1} - \mathbf{z}_{k+1} \quad (12c)$$

where

$$\tilde{\mathbf{x}}_k = \mathbf{z}_k - \mathbf{u}_k \quad (13a)$$

$$\tilde{\mathbf{z}}_k = \mathbf{x}_{k+1} + \mathbf{u}_k \quad (13b)$$

and  $\rho_k$  denotes the penalty parameter at the  $k$ -th iteration. In this way, the data fidelity term and the regularization term in (9) are decoupled into two sub-problems, (12a) and (12b). Sub-problem (12a) is a least square problem that can be solved analytically as follows:

$$\mathbf{x}_{k+1} = (\mathbf{H}^T \mathbf{H} + \rho_k \mathbf{I})^{-1} (\mathbf{H}^T \mathbf{y} + \rho_k \tilde{\mathbf{x}}_k) \quad (14)$$

Subproblem (12b) can be reformulated as:

$$\mathbf{z}_{k+1} = \arg \min_{\mathbf{z}} \frac{1}{2\sigma_k^2} \|\tilde{\mathbf{z}}_k - \mathbf{z}\|^2 + \Phi(\mathbf{z}) \quad (15)$$

where  $\sigma_k = \sqrt{\lambda/\rho_k}$ .

From a Bayesian perspective<sup>1</sup>, (15) can be considered as a denoising problem, removing Gaussian noise with noise-level  $\sigma_k$  from the noisy HSI  $\tilde{\mathbf{z}}_k$  to obtain the clean HSI  $\mathbf{z}_{k+1}$ . In other words, a denoising operator can be used for neglecting the design of the regularization term  $\Phi(\mathbf{x})$ .

### B. Estimating parameters via 3D residual whiteness

In most real-world applications, no ground-truth information is available for fine-tuning the algorithm parameters or terminating the optimization at a proper iteration. To tackle this issue, a measure of residual whiteness of 3D images is defined in this subsection, and the optimal value of  $\rho_k$  at each iteration, as well as the number of iterations, can be determined with the help of this measure. To be specific, we propose to evaluate the optimal  $\rho_k^*$  in (12a) by solving a scalar optimization problem. The stopping criterion then consists of comparing this 3D whiteness measure between two iterations.

1) *Measure of 3D residual whiteness*: We define the residual image  $\mathbf{r}_{k+1} \in \mathbb{R}^L$  with  $L = NPQ$  by:

$$\mathbf{r}_{k+1} = \mathbf{H}\mathbf{x}_{k+1} - \mathbf{y} \quad (16)$$

with its equivalent 3D image matrix denoted by  $\mathbf{R}_{k+1} \in \mathbb{R}^{N \times P \times Q}$ . The *auto-correlation* of  $\mathbf{R}_{k+1}$  is defined as:

$$\mathbf{A}_{\mathbf{R}_{k+1}} = \frac{1}{L} (\mathbf{R}_{k+1} * \mathbf{R}_{k+1}) \quad (17)$$

<sup>1</sup>Considering a degradation model  $\tilde{\mathbf{z}}_k = \mathbf{z} + \mathbf{n}_k$  where  $\mathbf{n}_k$  is Gaussian noise with standard deviation  $\sigma_k$ . The denoising problem can be formulated as the recovery of the posterior probability distribution function (PDF)  $p(\mathbf{z}|\tilde{\mathbf{z}}_k)$ . Using the Bayes theorem, this PDF can be written as:  $p(\mathbf{z}|\tilde{\mathbf{z}}_k) \propto p(\tilde{\mathbf{z}}_k|\mathbf{z})p(\mathbf{z})$  where  $p(\mathbf{z})$  is the prior probability distribution of  $\mathbf{z}$  and  $\propto$  means "proportional to". Finally, the log-posterior distribution can be written as  $-\log p(\mathbf{z}|\tilde{\mathbf{z}}_k) = \frac{1}{2\sigma_k^2} \|\tilde{\mathbf{z}}_k - \mathbf{z}\|^2 + \log p(\mathbf{z}) + C$  where  $C$  is a constant.

By rewriting  $\log p(\mathbf{z})$  as  $\Phi(\mathbf{z})$ , estimating  $\mathbf{z}$  in the sense of the maximum a posteriori principle leads to the optimization problem in (15).

where  $*$  denotes the 3D discrete correlation. The sample auto-correlation at indexes  $(n, p, q)$  is given by:

$$\mathbf{A}_{\mathbf{R}_{k+1}}(n, p, q) = \frac{1}{L} \sum_{m, i, j} \mathbf{R}_{k+1}(n, p, q) \mathbf{R}_{k+1}(m-n, i-p, j-q) \quad (18)$$

with  $1 \leq m \leq N$ ,  $1 \leq i \leq P$ ,  $1 \leq j \leq Q$ . When the residual is close to the modeling error  $\mathbf{n}$ , i.e., a white Gaussian noise,  $\mathbf{A}_{\mathbf{R}_{k+1}}(n, p, q)$  satisfies the following asymptotic property:

$$\lim_{L \rightarrow \infty} \mathbf{A}_{\mathbf{R}_{k+1}}(n, p, q) \approx \begin{cases} \sigma^2 & \text{if } (n, p, q) = (0, 0, 0) \\ 0 & \text{if } (n, p, q) \neq (0, 0, 0) \end{cases} \quad (19)$$

The size  $L$  of hyperspectral images is usually large (between  $10^6$  and  $10^8$ ), so that we can assume that the sample auto-correlation at all indexes  $(n, p, q) \neq (0, 0, 0)$  is close to zero. This assumption is based on the following result of the Gaussian process  $\mathbf{n}$  with its equivalent 3D image matrix denoted by  $\mathbf{N} \in \mathbb{R}^{N \times P \times Q}$  and sample auto-correlation  $\mathbf{A}_{\mathbf{N}_{k+1}}(n, p, q)$  defined by replacing  $\mathbf{R}$  as  $\mathbf{N}$  in (18).

**Theorem 1.** *If  $\mathbf{n}$  has a finite variance  $\sigma$  and  $L$  tends to  $\infty$ , any  $\mathbf{A}_{\mathbf{N}_{k+1}}(n, p, q)$  with  $(n, p, q) \neq (0, 0, 0)$  is asymptotically uncorrelated and Gaussian-distributed with zero mean and stand deviation  $\sigma_a = \sigma^2/L$*

*Proof.* The proof follows directly by applying Proposition 1 of [38] to the 3D domain.

The rational behind imposing residual whiteness is to estimate parameters by constraining the residual auto-correlation at non-zero indexes to be small. To make this measure independent from  $\sigma$ , inspired by [37], we consider the *normalized auto-correlation* defined as follows:

$$\bar{\mathbf{A}}_{\mathbf{R}_{k+1}} = \frac{\mathbf{A}_{\mathbf{R}_{k+1}}}{\mathbf{A}_{\mathbf{R}_{k+1}}(0, 0, 0)} = \frac{\mathbf{R}_{k+1} * \mathbf{R}_{k+1}}{\|\mathbf{R}_{k+1}\|_F^2} \quad (20)$$

where  $\|\cdot\|_F$  denotes the matrix Frobenius norm. All entries  $\bar{\mathbf{A}}_{\mathbf{R}_{k+1}}(n, p, q)$  satisfies:

$$\lim_{L \rightarrow \infty} \bar{\mathbf{A}}_{\mathbf{R}_{k+1}}(n, p, q) \approx \begin{cases} 1 & \text{if } (n, p, q) = (0, 0, 0) \\ 0 & \text{if } (n, p, q) \neq (0, 0, 0) \end{cases} \quad (21)$$

We can now introduce the  $\sigma$ -independent non-negative scalar measure of 3D residual whiteness defined as:

$$\mathcal{W}(\mathbf{R}_{k+1}) = \|\bar{\mathbf{A}}_{\mathbf{R}_{k+1}}\|_F^2 = \frac{\|\mathbf{R}_{k+1} * \mathbf{R}_{k+1}\|_F^2}{\|\mathbf{R}_{k+1}\|_F^4} \quad (22)$$

2) *Penalty parameter estimation*: Solution  $\mathbf{x}_{k+1}$  of (14) actually depends on parameter  $\rho_k$  setting. To devise the parameter selection procedure, we make  $\rho_k$  explicit by writing  $\mathbf{x}_{k+1, \rho_k}$ . In order to automatically estimate the penalty parameter  $\rho_k$  in (12a), the term  $\|\mathbf{x} - \tilde{\mathbf{x}}_k\|^2$  can be viewed as a regularizer that enforces the solution  $\mathbf{x}_{k+1, \rho_k}$  to tend to  $\tilde{\mathbf{x}}_k$ . As the restored image  $\mathbf{x}_{k+1, \rho_k}$  tends to fit the desired target image, the related residual image  $\mathbf{r}_{k+1, \rho_k} = \mathbf{H}\mathbf{x}_{k+1, \rho_k} - \mathbf{y}$  tends to be close to the Gaussian noise perturbation  $\mathbf{n}$  in (7). With (22), we propose to estimate the optimal penalty parameter by solving the following scalar optimization problem:

$$\rho_k^* = \arg \min_{\rho_k} \mathcal{W}(\mathbf{r}_{k+1, \rho_k}) \quad (23)$$

**Algorithm 1** Adaptive Penalty Parameter Estimation.

**Input:** Blurred observation  $\mathbf{y}$ , internal image  $\tilde{\mathbf{x}}_k$ , blurring kernel  $\mathbf{H}$ .

**Output:** Optimal adaptive parameter  $\rho_k^*$ .

Initialize  $a, b, \epsilon$ .

**while**  $b - a > \epsilon$  **do**

$$\rho_k^{(1)} = a + \delta(b - a)$$

$$\rho_k^{(2)} = b - \delta(b - a)$$

**if**  $\mathcal{W}(\mathbf{r}_{k+1, \rho_k^{(1)}}) < \mathcal{W}(\mathbf{r}_{k+1, \rho_k^{(2)}})$

$$b = \rho_k^{(2)}$$

**else**

$$a = \rho_k^{(1)}$$

**end while**

$$\rho_k^* = (a + b)/2$$

The varying range of  $\rho_k$  is  $(0, \infty)$ . In practice, we substitute the  $\infty$  by a sufficiently large value.

A fast golden-section search method is used for determining a local minimum of (23). This method operates iteratively over an interval  $(a, b)$  and generates two internal points:

$$\begin{aligned} \rho_k^{(1)} &= a + \delta(b - a) \\ \rho_k^{(2)} &= b - \delta(b - a) \end{aligned} \quad (24)$$

where  $\delta = 0.618$  is the golden ratio. As shown in Algorithm 1, whiteness criterion  $\mathcal{W}(\mathbf{r}_{k+1, \rho_k})$  is compared at  $\rho_k^{(1)}$  and  $\rho_k^{(2)}$ . If it is smaller at the former point than at the latter point, then  $b$  is substituted by  $\rho_k^{(2)}$ . Otherwise,  $a$  is substituted by  $\rho_k^{(1)}$ . This procedure is repeated with the new smaller interval  $(a, b)$  until  $b - a < \epsilon$  with  $\epsilon$  a small positive threshold. Finally, the estimated optimal penalty parameter is given by:

$$\rho_k^* = (a + b)/2 \quad (25)$$

and the solution of sub-problem (12a) is provided by:

$$\mathbf{x}_{k+1} = (\mathbf{H}^T \mathbf{H} + \rho_k^* \mathbf{I})^{-1} (\mathbf{H}^T \mathbf{y} + \rho_k^* \tilde{\mathbf{x}}_k) \quad (26)$$

3) *Stopping criterion:* To take both HSI deconvolution performance and computational time into account, it is important to properly set the maximum number of iterations. Iterations can be performed until no significant improvement between two consecutive iterations is observed. Considering the whiteness measure in (22), we propose to stop the iterative process with the following normalized criterion:

$$\mathcal{W}(\mathbf{r}_{k+1}) \geq \mathcal{W}(\mathbf{r}_k) \quad \text{or} \quad \frac{|\mathcal{W}(\mathbf{r}_{k+1}) - \mathcal{W}(\mathbf{r}_k)|}{\mathcal{W}(\mathbf{r}_{k+1})} < \zeta \quad (27)$$

where  $\zeta$  is a small positive threshold,  $\mathbf{r}_k$  and  $\mathbf{r}_{k+1}$  represent the residual image of the solutions  $\mathbf{x}_k$  and  $\mathbf{x}_{k+1}$ , respectively.

### C. Learning spectral-spatial priors via B3DDN

Instead of using a handcrafted regularizer  $\Phi(\cdot)$  and solving subproblem (12b) explicitly, we propose to carry out this task with a deep neural network based denoiser. This denoiser is trained beforehand to extract spectral-spatial prior information

from hyperspectral training observations. Then it is plugged into the iterative algorithm to solve subproblem (12b). We denote this denoising operator by  $\mathcal{D}(\cdot)$ . As it is performed in the 3D image domain to jointly capture spatial and spectral information, we write (15) as follows:

$$\mathbf{Z}_{k+1} = \mathcal{D}(\tilde{\mathbf{Z}}_k, \sigma_k) \quad (28)$$

Observe that  $\mathcal{D}(\cdot)$  is parameterized by the noise level  $\sigma_k$ . For setting it, most existing methods use empirical strategies that may lead to under-denoising or over-smoothing of  $\mathbf{Z}_k$  [23]. In addition, since  $\sigma_k$  decreases as iterations progress, some works choose to train a set of specific models that can handle different noise levels [22]. To avoid these redundant learning tasks, we shall now see how to design a blind 3D denoising network  $\mathcal{F}(\cdot)$  with respect to  $\sigma_k$ , but parameterised by  $\Theta$ , by considering residual learning formulation:

$$\mathbf{Z}_{k+1} = \tilde{\mathbf{Z}}_k - \mathcal{F}(\tilde{\mathbf{Z}}_k; \Theta) \quad (29)$$

1) *3D convolution:* Unlike 2D convolution resulting in spectral information distortion, 3D convolution extracts spatial features from neighboring pixels and spectral features from adjacent bands, simultaneously, without compromising spectral resolution. 3D convolution also involves less parameters, and it is more appropriate for hyperspectral image processing due to the difficulty in capturing a big enough volume of hyperspectral data. In addition, 3D convolution enables the neural network to handle HSIs with arbitrary number of spectral bands without modifying its architecture [39]. In this way, there is no need to retrain a neural network when the number of spectral bands changes. This key property allows our method to be applied to any real-world dataset by using a pre-trained neural network.

2) *Network architecture:* The B3DDN architecture is illustrated in Fig. 1 (top). Each 3D-block contains a 3D convolution layer (3DConv), a batch normalization (BN) layer and a ReLU layer. Batch normalization is used to speed up the training process as well as to boost the denoising performance [40]. Besides the input layer and the output layer, a 3D convolution layer (3DConv), a ReLU activation function layer,  $B$  3D-blocks and a last 3D convolution layer are sequentially connected to form the proposed network. The last convolutional layer contains one 3D-filter while the others are composed of 32 3D-filters. The kernel size of each 3D-filter is  $3 \times 3 \times 3$ , which means that the depth of the kernel along the spectral dimension and its size over the spatial dimension are 3 and  $3 \times 3$  respectively. Compared to existing complex network architectures for HSI denoising, B3DDN achieves satisfactory performance with less parameters. Moreover, it enables us to apply the neural network learned with simulated data, to real data that lacks ground truth. An example is provided in subsection IV-G.

3) *Learning strategy:* The input of the proposed B3DDN is a noisy hyperspectral image  $\tilde{\mathbf{z}} = \mathbf{z} + \mathbf{v}$ , where  $\mathbf{v}$  is a Gaussian noise with arbitrary standard deviation. Inspired by 2D image denoising algorithm [40], we consider the learning residual to predict the residual error  $\mathcal{F}(\tilde{\mathbf{z}}_k; \Theta) \approx \mathbf{v}$  in our denoising network. Then we can achieve the estimated clean image by

**Algorithm 2** Tuning-free HSI deconvolution with deep priors learnt from B3DDN.

**Input:** Network parameters  $\Theta$ , blurred observation  $\mathbf{y}$ , blurring kernel  $\mathbf{H}$ .

**Output:** Deblurred HSI  $\mathbf{X}$ .

Initialize  $\mathbf{x} = \mathbf{x}_0$ , auxiliary variable  $\mathbf{z}_0 = \mathbf{x}_0$ , scaled dual variable  $\mathbf{u}_0 = \mathbf{0}$ ,  $k = 0$ .

**while** Stopping criteria in (27) are not met **do**

$\tilde{\mathbf{x}}_k = \mathbf{z}_k - \mathbf{u}_k$

Estimate  $\rho_k^*$  using Algorithm 1

$\mathbf{x}_{k+1} = (\mathbf{H}^T \mathbf{H} + \mu \mathbf{I})^{-1} (\mathbf{H}^T \mathbf{y} + \rho_k^* \tilde{\mathbf{x}}_k)$

$\tilde{\mathbf{z}}_k = \mathbf{x}_{k+1} + \mathbf{u}_k$

$\mathbf{Z}_{k+1} = \tilde{\mathbf{Z}}_k - \mathcal{F}(\tilde{\mathbf{Z}}_k; \Theta)$

$\mathbf{u}_{k+1} = \mathbf{u}_k + \mathbf{x}_{k+1} - \mathbf{z}_{k+1}$

$k = k + 1$

**end while**

$\tilde{\mathbf{z}} - \mathcal{F}(\tilde{\mathbf{z}}; \Theta)$ . To train the blind neural network  $\mathcal{F}(\cdot; \Theta)$ , we use the following loss function:

$$\ell(\Theta) = \|\mathcal{F}(\tilde{\mathbf{z}}_m; \Theta) - (\tilde{\mathbf{z}}_m - \mathbf{z}_m)\|_1 \quad (30)$$

where  $\{(\tilde{\mathbf{z}}_m, \mathbf{z}_m)\}_{m=1}^M$  is a training set of generated noisy-clean HSI (patch) pairs with various noise levels. Note that the  $\ell_1$ -norm is used as a loss that is more robust to noise than the  $\ell_2$ -norm, found providing better performance in image restoration in the literature [35], [41]. After the B3DDN has been trained, it is incorporated into the ADMM framework as a blind denoiser, yielding Algorithm 2.

#### IV. EXPERIMENTS

In this section, we shall conduct experiments of HSI deconvolution on both simulated and real-world datasets to validate our method. The results provided by the proposed method are compared with those of several HSI deconvolution methods from both quantitative and qualitative perspectives. The source code and the proposed real-world data is made available at [https://github.com/xiuheng-wang/Tuning\\_free\\_PnP\\_HSI\\_deconvolution](https://github.com/xiuheng-wang/Tuning_free_PnP_HSI_deconvolution).

##### A. Simulation datasets and experimental setup

Two simulation datasets, on the one hand the Columbia Multispectral Database (CAVE)<sup>2</sup> [42], and on the other hand a remotely sensed hyperspectral data over Chikusei<sup>3</sup> [43], were used to evaluate the performance of our method.

1) *CAVE dataset*: The CAVE dataset contains 32 HSIs recorded under controlled illuminations in a laboratory. Each image has a spatial resolution of  $512 \times 512$  pixels, over 31 spectral channels ranging from 400 nm to 700 nm at a wavelength interval of 10 nm.

2) *Chikusei dataset*: The Chikusei dataset is an airborne hyperspectral scene acquired by a Visible and Near-Infrared imaging sensor over agricultural and urban regions in Chikusei, Ibaraki, Japan. The scene consists of  $2517 \times 2335$  pixels

with a ground sampling distance of 2.5 m, over 128 spectral channels ranging from 363 nm to 1018 nm. The black boundaries in the spatial domain were removed, leading to a scene of size  $2048 \times 2048$  pixels.

The HSIs of the two datasets were scaled to the range  $[0, 1]$ , and then used as ground truths for  $\mathbf{x}$ . The observations  $\mathbf{y}$  were generated by using the blurring kernels  $\mathbf{H}$  and corrupted with a white Gaussian noise  $\mathbf{n}$  with standard deviation  $\sigma$ , with  $\mathbf{H}$  and  $\sigma$  defined as follows; see Fig. 3:

- (a)  $9 \times 9$  Gaussian kernel with bandwidth 2, and  $\sigma = 0.01$ ;
- (b)  $13 \times 13$  Gaussian kernel with bandwidth 3, and  $\sigma = 0.01$ ;
- (c)  $9 \times 9$  Gaussian kernel with bandwidth 2, and  $\sigma = 0.03$ ;
- (d) Circle kernel with diameter 7, and  $\sigma = 0.01$ ;
- (e) Motion kernel from [44] of size  $13 \times 13$ , and  $\sigma = 0.01$ ;
- (f) Square kernel with side length 5, and  $\sigma = 0.01$ .

The first 20 images were selected from the CAVE dataset for training and the remaining 12 images were used for the test. For the Chikusei dataset, a  $1024 \times 2048$  sub-image was extracted from the top area of the image for training while the remaining part was cropped into 32 non-overlapping  $256 \times 256 \times 128$  sub-images that were used as test data.

##### B. Implementation details

We implemented the proposed blind denoising network B3DDN with PyTorch framework. The Adam optimizer [45] with an initial learning rate 0.0002 and batch size 64 was used to minimize the loss function (30) with 500 epochs. The weights were initialized by the method in [46]. At every epoch of the training stage, each original HSI was randomly cropped into 128 and 512 patches of size  $64 \times 64$  respectively for the CAVE and the Chikusei datasets. To train the B3DDN in a blind manner, we added an i.i.d. Gaussian noise with random standard deviation in the range  $[0.2, 10]$  to each patch, which was then randomly rotated or flipped for data augmentation purpose. We set the number  $B$  of 3D blocks to 8 by considering the computational cost and memory demand, and thus the number of parameters of the proposed B3DDN denoiser is 10113.

Once the denoiser was trained, assuming that the statistics of the test images differ from training images, we plugged the B3DDN into the ADMM. Since the computational complexity of 3D discrete correlation in (22) can be high ( $\mathcal{O}(L^2)$ ), we used the fast Fourier transform ( $\mathcal{O}(L \log L)$ ) to compute it. Step (26) was also efficiently computed in the Fourier domain. For the golden-section search method and the stopping criterion presented in Subsection III-B, we set  $a = 0$ ,  $b = 10$ ,  $\epsilon = 0.001$  and  $\zeta = 0.0002$ .

##### C. Quantitative metrics and baselines

In order to evaluate the quality of the deconvolution result  $\hat{\mathbf{X}}$  by comparing it with the ground truth of  $\mathbf{X}$ , we considered four quantitative metrics. The first one is the Root Mean-Square Error (RMSE), dedined as

$$\text{RMSE} = \sqrt{\frac{1}{NPQ} \sum_{i=1}^N \|\hat{\mathbf{X}}_i - \mathbf{X}_i\|_F^2},$$

<sup>2</sup><https://www1.cs.columbia.edu/CAVE/databases/multispectral/>

<sup>3</sup><http://naotoyokoya.com/Download.html>

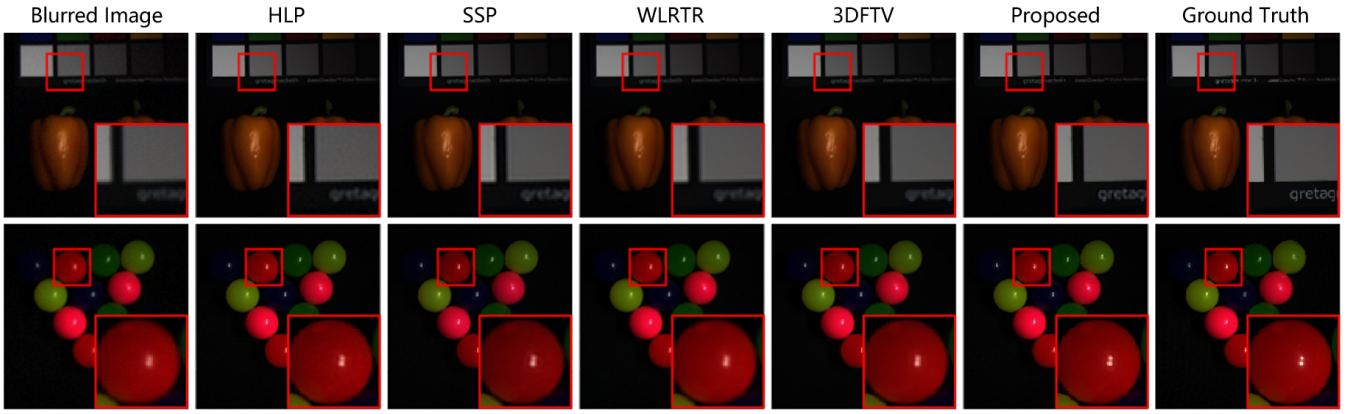


Fig. 2. Visual results for all methods in the blurring scenario (a) on the CAVE dataset. The first and second rows present the results for two different blurred images. The false color images were generated for clear visualization with the 22nd, 14th and 7th channels used for red, green and blue, respectively.

TABLE I  
RMSE, PSNR, SSIM AND ERGAS OF THE DIFFERENT METHODS APPLIED TO THE CAVE DATASET IN THE 6 BLURRING SCENARIOS.

Scenarios	Metrics	HLP	SSP	WLRTR	3DFTV	Ours
(a)	RMSE	4.420 ± 1.787	4.848 ± 1.825	4.735 ± 2.076	4.332 ± 1.863	<b>3.132 ± 1.320</b>
	PSNR	36.166 ± <b>3.334</b>	35.373 ± 3.385	35.872 ± 3.759	36.450 ± 3.793	<b>39.252 ± 3.465</b>
	SSIM	0.9167 ± 0.0379	0.9305 ± 0.0393	0.9380 ± 0.0466	0.9401 ± 0.0439	<b>0.9493 ± 0.0367</b>
	ERGAS	18.15 ± 8.25	19.51 ± 8.12	18.96 ± 8.33	17.34 ± 7.69	<b>13.01 ± 6.23</b>
(b)	RMSE	5.707 ± 2.452	5.955 ± 2.398	6.439 ± 2.812	5.667 ± 2.539	<b>4.581 ± 1.993</b>
	PSNR	34.034 ± 3.567	33.541 ± <b>3.492</b>	33.084 ± 3.740	34.116 ± 3.872	<b>36.305 ± 3.612</b>
	SSIM	0.8911 ± 0.0483	0.9031 ± 0.0494	0.9025 ± 0.0616	0.9136 ± 0.550	<b>0.9234 ± 0.0422</b>
	ERGAS	22.92 ± 10.11	23.71 ± 9.86	25.46 ± 10.84	22.40 ± 9.86	<b>18.54 ± 8.39</b>
(c)	RMSE	7.669 ± 1.390	5.270 ± 1.622	5.099 ± 1.972	5.016 ± 1.727	<b>4.225 ± 1.324</b>
	PSNR	30.599 ± <b>1.550</b>	34.309 ± 2.607	34.827 ± 3.201	34.741 ± 2.975	<b>36.211 ± 2.485</b>
	SSIM	0.6406 ± 0.0337	0.8565 ± 0.0539	<b>0.8956 ± 0.0387</b>	0.8851 ± 0.0390	0.8708 ± 0.0594
	ERGAS	33.49 ± 16.27	22.28 ± 10.14	20.80 ± <b>9.07</b>	20.47 ± 8.66	<b>18.64 ± 9.28</b>
(d)	RMSE	4.189 ± 1.636	4.584 ± 1.680	4.328 ± 1.903	4.167 ± 1.803	<b>2.305 ± 0.938</b>
	PSNR	36.548 ± 3.181	35.862 ± 3.331	36.686 ± 3.736	36.805 ± 3.803	<b>41.653 ± 3.074</b>
	SSIM	0.9165 ± 0.0348	0.9354 ± 0.0374	0.9450 ± 0.0436	0.9403 ± 0.0430	<b>0.9542 ± 0.0340</b>
	ERGAS	17.36 ± 7.98	18.49 ± 7.67	17.45 ± 7.82	16.69 ± 7.46	<b>9.86 ± 5.17</b>
(e)	RMSE	3.759 ± 1.166	3.954 ± <b>1.333</b>	4.335 ± 1.780	3.587 ± 1.443	<b>3.041 ± 2.783</b>
	PSNR	37.149 ± <b>2.492</b>	37.160 ± 3.108	36.497 ± 3.490	37.991 ± 3.543	<b>40.722 ± 5.730</b>
	SSIM	0.9118 ± <b>0.0239</b>	<b>0.9472 ± 0.0311</b>	0.9428 ± 0.0436	0.9510 ± 0.0397	0.8907 ± 0.1642
	ERGAS	15.94 ± 7.39	16.01 ± <b>6.56</b>	17.46 ± 7.49	14.37 ± 6.16	<b>15.56 ± 19.66</b>
(f)	RMSE	3.971 ± 1.453	4.356 ± 1.563	4.109 ± 1.765	3.957 ± 1.666	<b>2.280 ± 1.231</b>
	PSNR	36.910 ± <b>2.985</b>	36.322 ± 3.302	37.130 ± 3.698	37.225 ± 3.743	<b>41.932 ± 3.687</b>
	SSIM	0.9195 ± 0.0270	0.9397 ± 0.334	0.9480 ± 0.0450	0.9468 ± 0.0410	<b>0.9475 ± 0.0618</b>
	ERGAS	16.58 ± 7.61	17.60 ± 7.26	16.64 ± 7.46	15.89 ± 7.04	<b>9.79 ± 5.89</b>

The best results are indicated by boldface numbers.

which measures the similarities between the deconvolution image and the reference image. A lower RMSE value indicates better quality. The second metric is the Peak-Signal-to-Noise-Ratio (PSNR):

$$\text{PSNR} = \frac{1}{N} \sum_{i=1}^N 10 \log_{10} \left( \frac{PQ \max(\mathbf{X}_i)^2}{\|\hat{\mathbf{X}}_i - \mathbf{X}_i\|_F^2} \right),$$

which measures the quality of the deconvolution image compared to the original image. The higher the PSNR, the better quality. The third metric is the average of Structural Similarity

(SSIM) [47], averaged over all channels of  $\hat{\mathbf{X}}$  and  $\mathbf{X}$ , i.e.,

$$\text{SSIM} = \frac{1}{N} \sum_{i=1}^N \frac{(2\mu_{\hat{\mathbf{X}}_i} \mu_{\mathbf{X}_i} + C_1)(2\sigma_{\hat{\mathbf{X}}_i \mathbf{X}_i} + C_2)}{(\mu_{\hat{\mathbf{X}}_i} + \mu_{\mathbf{X}_i} + C_1)(\sigma_{\hat{\mathbf{X}}_i} + \sigma_{\mathbf{X}_i} + C_2)},$$

where  $\mu_{\hat{\mathbf{X}}_i}$  and  $\mu_{\mathbf{X}_i}$  are the mean values of images  $\hat{\mathbf{X}}_i$  and  $\mathbf{X}_i$ ,  $\sigma_{\hat{\mathbf{X}}_i}$  and  $\sigma_{\mathbf{X}_i}$  are the standard deviations of  $\hat{\mathbf{X}}_i$  and  $\mathbf{X}_i$ ,  $\sigma_{\hat{\mathbf{X}}_i \mathbf{X}_i}$  is the covariance of  $\hat{\mathbf{X}}_i$  and  $\mathbf{X}_i$ , and  $C_1 > 0$  and  $C_2 > 0$  are constants. The SSIM is an indicator of the spatial structure preservation of the deconvolution image. A higher

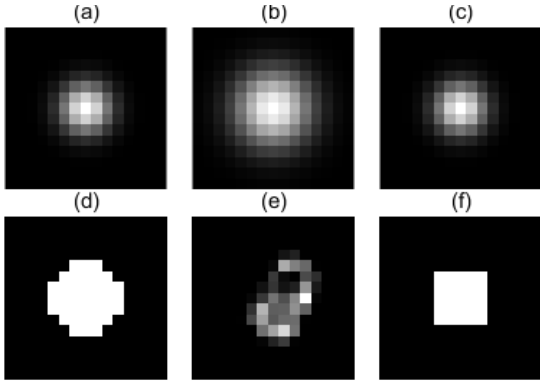


Fig. 3. Blurring kernels used for the experiments: (a)-(c) are Gaussian kernels, (d)-(f) are circle, motion and square kernels respectively.

TABLE II  
RMSE, PSNR, SSIM AND ERGAS OF THE DIFFERENT METHODS APPLIED TO THE CAVE DATASET IN THE BLURRING SCENARIO (A) WITH VARIOUS NOISE LEVELS.

$\sigma$	Methods	RMSE	PSNR	SSIM	ERGAS
0.01	HLP	4.420	36.166	0.9167	18.15
	SSP	4.848	35.373	0.9305	19.51
	WLRTR	4.735	35.872	0.9380	18.96
	3DFTV	4.332	36.450	0.9401	17.34
	Ours	<b>3.132</b>	<b>39.252</b>	<b>0.9493</b>	<b>13.01</b>
0.02	HLP	5.597	33.571	0.8084	23.77
	SSP	5.001	34.951	0.8973	20.52
	WLRTR	4.817	35.602	0.9283	19.39
	3DFTV	4.486	36.006	<b>0.9301</b>	17.96
	Ours	<b>3.574</b>	<b>37.851</b>	0.9140	<b>15.17</b>
0.03	HLP	7.669	30.599	0.6406	33.49
	SSP	5.270	34.309	0.8565	22.28
	WLRTR	5.099	34.827	<b>0.8956</b>	20.80
	3DFTV	5.016	34.741	0.8851	20.47
	Ours	<b>4.225</b>	<b>36.211</b>	0.8708	<b>18.64</b>
0.04	HLP	10.018	28.206	0.4942	44.43
	SSP	5.643	33.547	0.8155	24.66
	WLRTR	6.611	32.107	0.7539	27.42
	3DFTV	6.143	32.682	0.7778	26.05
	Ours	<b>4.750</b>	<b>35.060</b>	<b>0.8324</b>	<b>21.37</b>
0.05	HLP	12.411	26.320	0.3859	55.50
	SSP	6.101	32.742	0.7766	27.49
	WLRTR	9.496	28.748	0.5363	40.74
	3DFTV	7.696	30.572	0.6462	33.57
	Ours	<b>5.329</b>	<b>33.976</b>	<b>0.7984</b>	<b>24.60</b>

The best results are indicated by boldface numbers.

the SSIM value indicates better spatial structure preservation. The last metric is the Erreur Relative Globale Adimensionnelle de Synthèse (ERGAS) [48] defined as

$$\text{ERGAS} = 100 \sqrt{\frac{1}{N} \sum_{i=1}^N \frac{\|\hat{\mathbf{X}}_i - \mathbf{X}_i\|_F^2}{\text{mean}(\hat{\mathbf{X}}_i)^2}},$$

which characterizes the overall quality of the deconvolution image. A smaller ERGAS means a better result.

We compared our method with three HSI deconvolution methods of reference: hyper-laplacian priors (HLP) [49], spatial and spectral priors (SSP) [14], weighted low-rank tensor recovery (WLRTR) [15], 3D fractional total variation (3DFTV) [50], each with well-designed regularizers. The HLP considers spatial gradient priors, i.e., the hyper-Laplacian priors of images. The SSP exploits both the spatial and spectral smoothness priors of hyperspectral images. The WLRTR simultaneously captures non-local similarity within spectral-spatial cubic and spectral correlation by a low-rank tensor recovery model. The 3DFTV exploits both the local and non-local smoothness of images in all dimensions. We used the codes provided by the authors of these methods and downloaded them, and we tuned their parameters by following the rules as stated in the corresponding papers to achieve the best deconvolution performance.

#### D. Performance evaluation on simulated data

We start validating the tuning-free scheme with the CAVE dataset by demonstrating its effectiveness in terms of HSI deconvolution performance over the other methods.

Table I reports the average values and standard deviations of RMSE, PSNR, SSIM and ERGAS. For all blurring scenarios, one can observe that our method outperformed all competing methods in terms of performance and robustness. For quality comparison, consider scenario (a) for example. Fig. 2 provides the blurred image, deblurred images, ground truth of *real and fake peppers* (first row) and *superballs* (second row) from the CAVE dataset. Visually, our method provides more details, including sharper edges and more vivid gloss. This confirms the effectiveness of the proposed method in recovering the spatial information of the latent clear HSIs. To further evaluate the robustness of the proposed method, consider scenario (a) for example. We set the noise level from 0.01 to 0.05 at an interval of 0.01 to generate varying noise interruptions added to input images. In Table IV-A2, it can be seen that the performance of all methods deteriorates with the increase in noise levels. However, the proposed method still provides the best quantitative results with all different noise interruptions.

We now evaluate the proposed method on remotely sensed data: the Chikusei dataset. This dataset, with more spectral bands, allows to analyze how our method exploits spectral information. The mean and variance of the numerical results for all methods in 6 blurring scenarios are provided in Table III. It can be observed that the quantitative metrics of our method surpass the other competing methods in most cases. Fig. 4 displays the visual results. As can be seen, the proposed method provides results with clearer and sharper visual effects compared to the other methods. This illustrates the superiority of our method in recovering the latent HSIs with more spectral bands.

#### E. Convergence illustration

In many PnP algorithms for inverse imaging problems, the ADMM is widely used as a variable splitting technique. In some works, the convergence of PnP schemes based on some linear denoisers, including Non-Local Means (NLM) [51]



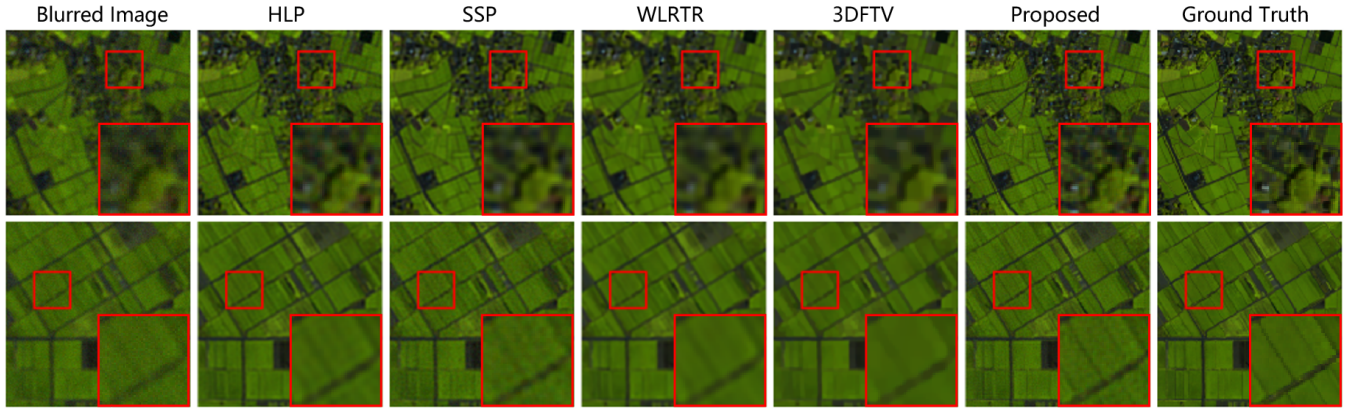


Fig. 4. Visual results for all methods with the blurring scenario (d) applied to the Chikusei dataset. The first and second rows present the results for two different images. The false color images were generated for clear visualization with the 122nd, 84th and 57th channels used for red, green and blue, respectively.

TABLE III  
RMSE, PSNR, SSIM AND ERGAS OF THE DIFFERENT METHODS APPLIED TO THE CHIKUSEI DATASET IN THE 6 BLURRING SCENARIOS.

Scenarios	Metrics	HLP	SSP	WLRTR	3DFTV	Ours
(a)	RMSE	3.233 ± 0.420	3.050 ± 0.452	3.138 ± 0.518	3.207 ± 0.501	<b>2.560 ± 0.316</b>
	PSNR	38.979 ± 1.131	40.182 ± 1.528	40.051 ± 1.710	39.546 ± 1.583	<b>41.032 ± 1.076</b>
	SSIM	0.9124 ± 0.0141	0.9334 ± 0.0148	0.9267 ± 0.0183	0.9171 ± 0.0191	<b>0.9420 ± 0.0086</b>
	ERGAS	32.25 ± 3.40	28.13 ± <b>2.64</b>	<b>25.29</b> ± 3.54	35.37 ± 2.93	27.87 ± 2.84
(b)	RMSE	3.945 ± 0.576	3.819 ± 0.566	4.091 ± 0.678	4.037 ± 0.644	<b>3.428 ± 0.502</b>
	PSNR	37.604 ± <b>1.348</b>	38.392 ± 1.573	37.872 ± 1.741	37.708 ± 1.637	<b>38.989</b> ± 1.438
	SSIM	0.8822 ± 0.0227	0.9016 ± 0.0222	0.8871 ± 0.0276	0.8819 ± 0.0275	<b>0.9091 ± 0.0183</b>
	ERGAS	35.30 ± 4.08	32.40 ± 3.60	31.45 ± 4.97	39.85 ± 3.59	<b>30.92 ± 3.23</b>
(c)	RMSE	7.094 ± <b>0.197</b>	3.506 ± 0.386	3.777 ± 0.429	3.662 ± 0.416	<b>3.413</b> ± 0.295
	PSNR	31.391 ± <b>0.252</b>	<b>37.942</b> ± 0.930	37.447 ± 0.955	37.756 ± 0.994	37.934 ± 0.703
	SSIM	0.6268 ± <b>0.0060</b>	0.8839 ± 0.0146	0.8816 ± 0.0157	<b>0.8841</b> ± 0.0152	0.8783 ± 0.0113
	ERGAS	90.14 ± 11.92	50.26 ± 6.80	<b>39.95</b> ± <b>4.34</b>	48.15 ± 5.01	51.38 ± 7.55
(d)	RMSE	3.361 ± <b>0.177</b>	2.879 ± 0.427	2.890 ± 0.477	3.076 ± 0.483	<b>2.335</b> ± 0.202
	PSNR	39.122 ± 0.995	40.625 ± 1.505	40.724 ± 1.689	39.900 ± 1.587	<b>41.290 ± 0.729</b>
	SSIM	0.9148 ± 0.0114	0.9399 ± 0.0132	0.9364 ± 0.0160	0.9228 ± 0.0178	<b>0.9430 ± 0.0045</b>
	ERGAS	32.76 ± 3.47	27.22 ± <b>2.47</b>	<b>23.73</b> ± 3.17	34.59 ± 2.86	32.56 ± 3.76
(e)	RMSE	2.960 ± 0.253	2.436 ± 0.352	2.790 ± 0.460	2.797 ± 0.436	<b>1.995 ± 0.106</b>
	PSNR	39.127 ± 0.681	41.869 ± 1.380	41.025 ± 1.644	40.574 ± 0.534	<b>42.207 ± 0.468</b>
	SSIM	0.9147 ± 0.0055	<b>0.9558</b> ± 0.0090	0.9408 ± 0.0147	0.9338 ± 0.0149	0.9507 ± <b>0.0028</b>
	ERGAS	35.79 ± 4.15	25.42 ± <b>2.14</b>	<b>23.09</b> ± 2.90	33.56 ± 2.96	36.06 ± 4.93
(f)	RMSE	2.990 ± 0.327	2.688 ± 0.395	2.691 ± 0.441	2.913 ± 0.453	<b>2.148 ± 0.186</b>
	PSNR	39.352 ± 0.902	41.174 ± 1.473	41.313 ± 1.659	40.334 ± 1.561	<b>41.971 ± 0.694</b>
	SSIM	0.9188 ± 0.0093	0.9456 ± 0.0116	0.9438 ± 0.0140	0.9295 ± 0.0161	<b>0.9506 ± 0.0038</b>
	ERGAS	32.68 ± 3.53	26.19 ± <b>2.29</b>	<b>22.46</b> ± 2.89	33.74 ± 2.82	30.62 ± 3.68

The best performance results are indicated by boldface numbers.

and Gaussian Mixture Model (GMM) [52], has been proved theoretically. It is difficult if not impossible to prove the convergence of our method as the B3DDN denoiser involves amounts of non-linear operators. In practice, however, as illustrated below, we observed that the proposed deconvolution framework shows good convergence behaviour.

Figure 5 provides the mean RMSE curves of our algorithm obtained for the CAVE dataset in the case of scenarios (a), (b) and (c). It can be observed that the algorithm, even with its nonlinear B3DDN denoiser, exhibits a stable and robust

convergence behaviour independently of the blurring kernel and noise level. Moreover, a low mean RMSE value was reached after few iterations, which indicates that early stopping can be considered to limit computation time.

#### F. Behavior with respect to PnP internal parameter estimation

Deep priors that capture both the spatial context and spectral correlations of the latent clean HSIs mainly contribute to the effectiveness of our method. But the internal parameter setting procedure and the stopping criterion also play a crucial role in

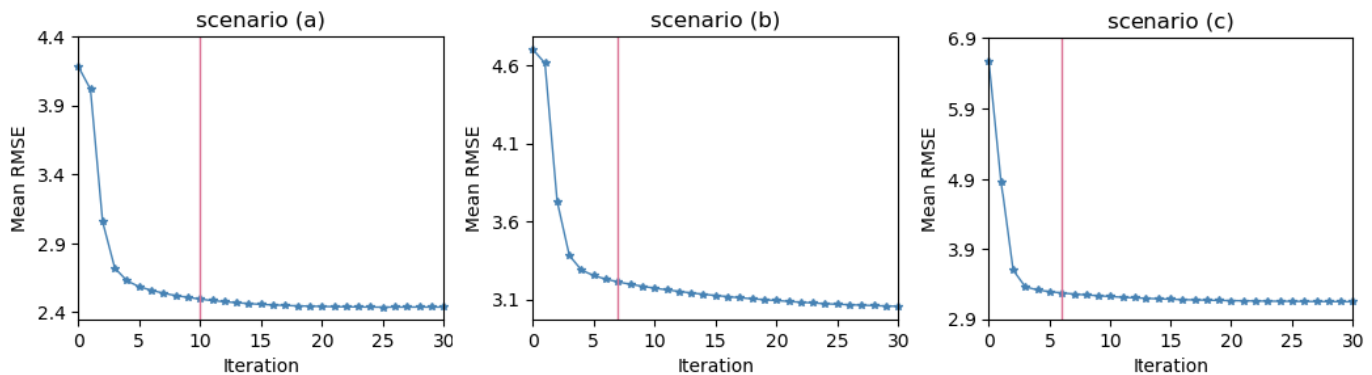


Fig. 5. RMSE convergence mean curves (blue) of our method with the CAVE dataset and blurring scenarios (a), (b) and (c). Red lines represent the iteration number given by the proposed stopping criterion.

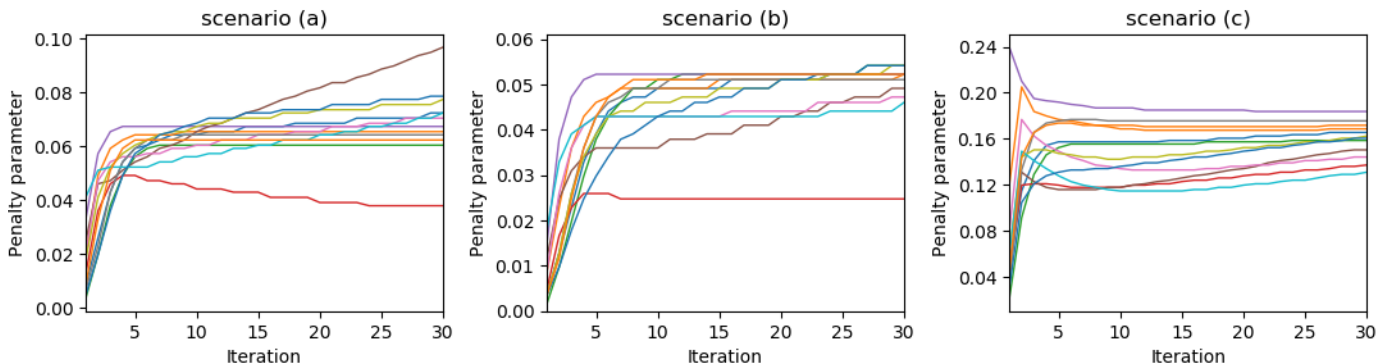


Fig. 6. Estimated penalty parameters  $\rho_k$  as a function of iteration index  $k$ , for different images of the CAVE dataset and blurring scenarios (a), (b) and (c). Lines with different colors refer to different test images.

achieving satisfactory performance by yielding a good balance with the contribution of deep priors. In contrast, observe that the automatic setting of the regularization parameters is not implemented by the other competing methods during test.

Fig. 6 shows how the penalty parameter varies along with the iterations, for different images of the CAVE dataset, and for scenarios (a), (b), and (c). According to the PnP principle, the estimated noise level  $\sigma_k$  is assumed to decrease along with the iterations, as the reconstructed image converges to a desired point. Therefore, the penalty parameter  $\rho_k = \lambda/\sigma_k^2$  is expected to increase [24]. As can be seen on Fig. 6, parameter  $\rho$  changes coincide with this trend for almost all test images. Fig. 5 shows the number of iterations  $K$  for scenarios (a), (b) and (c). It can be observed that our stopping criterion automatically interrupts the PnP algorithm when it has nearly converged, which contributes to save computation time.

### G. Performance evaluation on real-world data

To validate the effectiveness of our method in real-world conditions, we collected six unfocused HSIs and the corresponding focused images for different indoor and outdoor scenes. Specifically, as illustrated in Fig. 8, the HSIs of the indoor scenes were recorded under controlled illuminations while the outdoor HSIs were captured under normal daylight illumination. To fully capture the complex blurs caused by the imaging system, our dataset was elaborated to address hyperspectral deconvolution problem with respect

to defocus. In particular, blurred images were obtained by making the camera out of focus while clear references were also captured by focusing the camera. We captured these images with the GaiaField systems (see details in [53]) of our laboratory at Northwestern Polytechnical University. The GaiaField (Jiangsu Dualix Spectral Image Technology Co. Ltd., GaiaField-V10) is a push-broom imaging spectrometer with an HSIA-OL50 lens, covering the visible and NIR wavelengths ranging from 373.70 to 1000.90 nm, with a spectral resolution of 4.6 nm (129 channels in total). The spatial resolution of the images is  $780 \times 696$  pixels.

For all acquired images, we conducted a pre-processing procedure as described in [54]. First, we removed over-noisy and over-exposed bands. We got 45 exploitable bands, which were normalized such that the 0.999 intensity quantile corresponded to the value 1. Then, all HSIs were denoised using the approach described in [55] to enhance images. Blurred images and their clear counterparts are illustrated in the first and second columns of Fig. 7, respectively. Note that these image pairs are not strictly aligned due to multiple factors affecting the camera mounting. The clear images were used for visual comparisons only. The blurring kernel in each channel was estimated using the method described in [56]. For illustration purpose, Fig. 9 shows the kernels in the 10th, 20th, 30th and 40th channels of the blurred images *fruit* and *bicycle*. For all experiments, we added an i.i.d. Gaussian noise to the blurred images, with a signal-to-noise ratio (SNR) set to 40 dB.

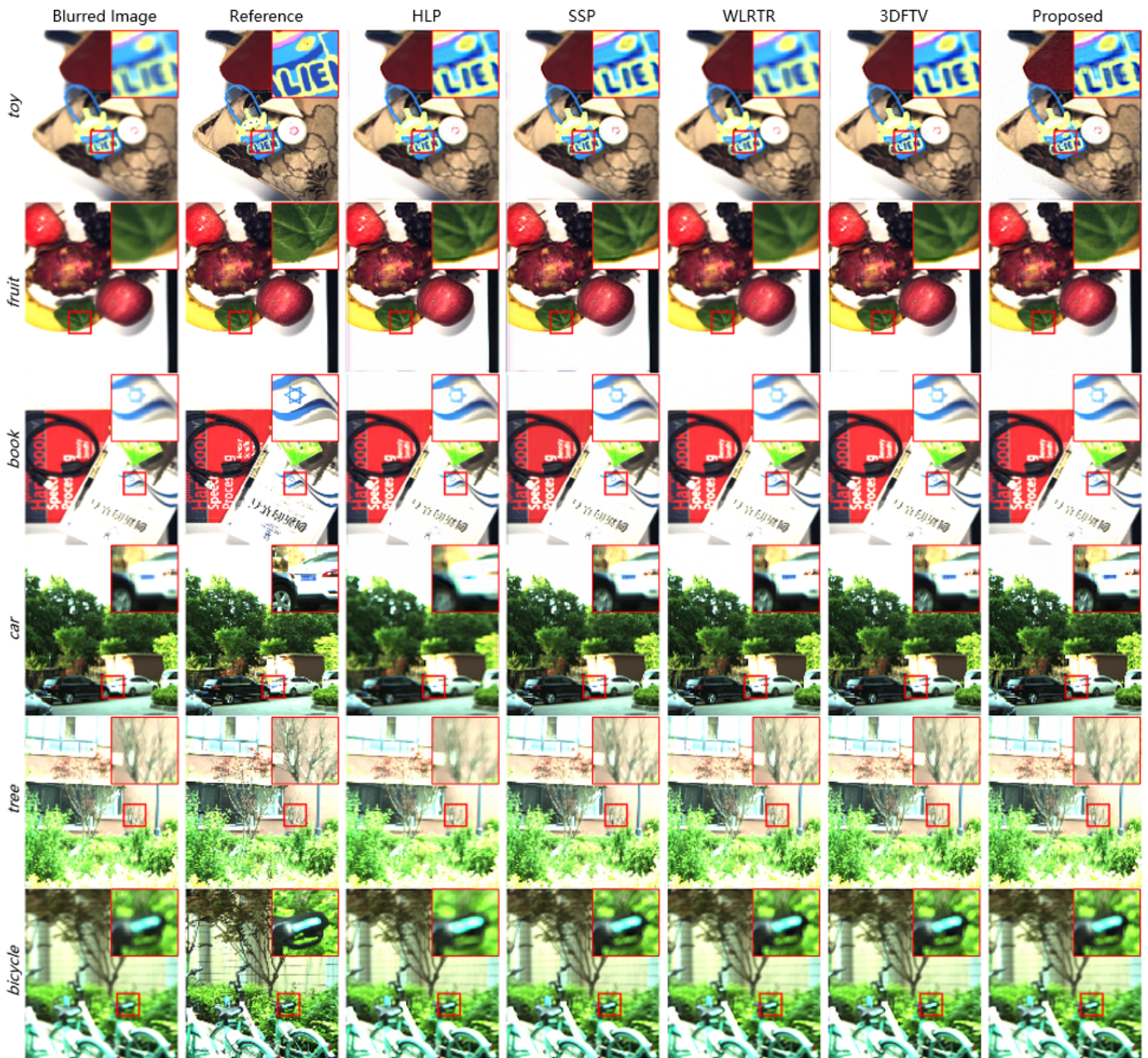


Fig. 7. Blurred images, reference images and visual results for all methods on the real-world dataset. The false color images were generated for clear visualization with the 38th, 24th and 10th channels used for red, green and blue, respectively.



Fig. 8. Indoor (left) and outdoor (right) experimental setups for collecting real data.

In real-world HSI deconvolution scenarios, no ground truth is available for training the B3DDN. Benefiting from the flexibility of the B3DDN in denoising HSIs of various origins

with distinct numbers of spectral bands, in this experiment we used the network parameters  $\Theta$  learned with the CAVE dataset (31 spectral bands). Fig. 7 shows the deblurred images obtained with all the competing algorithms, from columns 3 to 7. It can be seen that our method still performed better, or similarly, in recovering details compared to HLP, SSP, WLRTR, and 3DFTV, though all competing methods only achieved limited performance probably due to deviations in estimating kernels. This demonstrates the applicability of our method in real-world scenarios, as well as the necessity of further investigating blind hyperspectral deconvolution algorithms.

Finally, we conducted the experiment for evaluating the running time using the blurred image *fruit* from our real-world

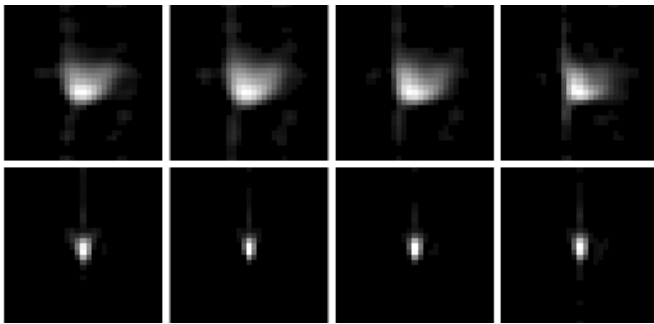


Fig. 9. Estimated blurring kernels in the 10th, 20th, 30th and 40th channels of the blurred images *fruit* (first row) and *bicycle* (second row) of the real-world dataset.

TABLE IV

TIME CONSUMING OF THE COMPARED METHODS FOR THE BLURRED IMAGE *fruit* OF THE REAL-WORLD DATASET.

	HLP	SSP	WLTR	3DFTV	Ours
Time (sec)	9.7	622.5	10501.2	6044.4	4280.6

dataset. All the baselines were implemented using MATLAB while our method was carried out using Python. We conducted all the experiments on a server with Intel Xeon Gold 6152 CPU, 512-GB random access memory and NVIDIA Tesla P40 GPU. Time consuming of all the compared methods is shown in Table IV. It can be observed that our method achieves most competitive deconvolution results with relatively less computation time.

## V. CONCLUSION

In this paper we presented a tuning-free HSI deconvolution method based on the PnP framework. Instead of using handcrafted priors, we designed a blind B3DDN denoiser based on deep learning to learn the spectral-spatial information of hyperspectral images from data and plugged it into an ADMM optimizer. The internal parameters were automatically estimated by a measure of 3D residual whiteness and learned by the B3DDN during iterations. Experimental results demonstrated that the proposed method can not only effectively handle various simulated blurring settings but can also be applied to real-world scenarios. In the future, we will address blind HSI deconvolution and computational cost reduction to further enhance the applicability of our method in real-world scenarios.

## REFERENCES

- [1] X. Wang, J. Chen, C. Richard, and D. Brie, "Learning spectral-spatial prior via 3DDnCNN for hyperspectral image deconvolution," in *Proc. IEEE Int. Conf. on Acoust. Speech, Signal Process (ICASSP)*. IEEE, 2020, pp. 2403–2407.
- [2] J. M. Bioucas-Dias, A. Plaza, G. Camps-Valls, P. Scheunders, N. Nasrabadi, and J. Chanussot, "Hyperspectral remote sensing data analysis and future challenges," *IEEE Geosci. Remote Sens. Mag.*, vol. 1, no. 2, pp. 6–36, 2013.
- [3] L. Yan, M. Zhao, X. Wang, Y. Zhang, and J. Chen, "Object detection in hyperspectral images," *IEEE Signal Process. Lett.*, vol. 28, pp. 508–512, 2021.
- [4] S. Bongard, F. Soulez, É. Thiébaud, and É. Pecontal, "3d deconvolution of hyper-spectral astronomical data," *Mon. Not. Roy. Astron. Soc.*, vol. 418, no. 1, pp. 258–270, 2011.
- [5] P. Sarder and A. Nehorai, "Deconvolution methods for 3-d fluorescence microscopy images," *IEEE Signal Process. Mag.*, vol. 23, no. 3, pp. 32–45, 2006.
- [6] N. P. Galatsanos and R. T. Chin, "Digital restoration of multichannel images," *IEEE Trans. Audio, Speech, Language Process.*, vol. 37, no. 3, pp. 415–421, 1989.
- [7] B. Hunt and O. Kubler, "Karhunen-loeve multispectral image restoration, part i: Theory," *IEEE Trans. Audio, Speech, Language Process.*, vol. 32, no. 3, pp. 592–600, 1984.
- [8] A. M. Tekalp and G. Pavlović, "Multichannel image modeling and kalman filtering for multispectral image restoration," *Signal Process.*, vol. 19, no. 3, pp. 221–232, 1990.
- [9] N. P. Galatsanos, A. K. Katsaggelos, R. T. Chin, and A. D. Hillery, "Least squares restoration of multichannel images," *IEEE Trans. Signal Process.*, vol. 39, no. 10, pp. 2222–2236, 1991.
- [10] J.-M. Gaucel, M. Guillaume, and S. Bourennane, "Adaptive-3d-wiener for hyperspectral image restoration: Influence on detection strategy," in *Proc. EUSIPCO*, 2006, pp. 1–5.
- [11] E. Thiébaud, "Introduction to image reconstruction and inverse problems," in *Proc. NATO Adv. Study Inst. Opt. Astrophys.*, 2005, pp. 1–26.
- [12] R. Neelamani, H. Choi, and R. Baraniuk, "Forward: Fourier-wavelet regularized deconvolution for ill-conditioned systems," *IEEE Trans. Signal Process.*, vol. 52, no. 2, pp. 418–433, 2004.
- [13] Y. Song, E.-H. Djermoune, J. Chen, C. Richard, and D. Brie, "Online deconvolution for industrial hyperspectral imaging systems," *SIAM J. Imaging Sci.*, vol. 12, no. 1, pp. 54–86, 2019.
- [14] S. Henrot, C. Soussen, and D. Brie, "Fast positive deconvolution of hyperspectral images," *IEEE Trans. Image Process.*, vol. 22, no. 2, pp. 828–833, 2012.
- [15] Y. Chang, L. Yan, X.-L. Zhao, H. Fang, Z. Zhang, and S. Zhong, "Weighted low-rank tensor recovery for hyperspectral image restoration," *IEEE Trans. Cybern.*, vol. 50, no. 11, pp. 4558–4572, 2020.
- [16] S. Boyd, N. Parikh, E. Chu, B. Peleato, J. Eckstein *et al.*, "Distributed optimization and statistical learning via the alternating direction method of multipliers," *Found. Trends Mach. Learn.*, vol. 3, no. 1, pp. 1–122, 2011.
- [17] D. Geman and C. Yang, "Nonlinear image recovery with half-quadratic regularization," *IEEE Trans. Image Process.*, vol. 4, no. 7, pp. 932–946, 1995.
- [18] J. Chen, M. Zhao, X. Wang, C. Richard, and S. Rahardja, "Integration of physics-based and data-driven models for hyperspectral image unmixing," *IEEE Signal Process. Mag.*, 2022.
- [19] K. Wei, A. Aviles-Rivero, J. Liang, Y. Fu, C.-B. Schönlieb, and H. Huang, "Tuning-free plug-and-play proximal algorithm for inverse imaging problems," in *Proc. Int. Conf. Mach. Learn. (ICML)*. PMLR, 2020, pp. 10 158–10 169.
- [20] S. V. Venkatakrisnan, C. A. Bouman, and B. Wohlberg, "Plug-and-play priors for model based reconstruction," in *Proc. IEEE Glob. Conf. Signal. Inf. Process.*, 2013, pp. 945–948.
- [21] A. Brifman, Y. Romano, and M. Elad, "Turning a denoiser into a super-resolver using plug and play priors," in *Proc. IEEE Int. Conf. Image Process. (ICIP)*, 2016, pp. 1404–1408.
- [22] K. Zhang, W. Zuo, S. Gu, and L. Zhang, "Learning deep cnn denoiser prior for image restoration," in *Proc. IEEE Conf. Comput. Vis. Pattern Recognit. (CVPR)*, 2017, pp. 3929–3938.
- [23] M. Chen, Y. Chang, S. Cao, and L. Yan, "Learning blind denoising network for noisy image deblurring," in *Proc. IEEE Int. Conf. on Acoust. Speech, Signal Process (ICASSP)*. IEEE, 2020, pp. 2533–2537.
- [24] K. Zhang, Y. Li, W. Zuo, L. Zhang, L. Van Gool, and R. Timofte, "Plug-and-play image restoration with deep denoiser prior," *IEEE Trans. Pattern Anal. Mach. Intell.*, 2021.
- [25] X. Wang, M. Zhao, and J. Chen, "Hyperspectral unmixing via plug-and-play priors," in *Proc. IEEE Int. Conf. Image Process. (ICIP)*. IEEE, 2020, pp. 1063–1067.
- [26] M. Zhao, X. Wang, J. Chen, and W. Chen, "A plug-and-play priors framework for hyperspectral unmixing," *IEEE Trans. Geosci. Remote Sens.*, 2021.
- [27] A. M. Thompson, J. C. Brown, J. W. Kay, and D. M. Titterton, "A study of methods of choosing the smoothing parameter in image restoration by regularization," *IEEE Trans. Pattern Anal. Mach. Intell.*, vol. 13, no. 04, pp. 326–339, 1991.
- [28] P. C. Hansen, "Analysis of discrete ill-posed problems by means of the l-curve," *SIAM Rev.*, vol. 34, no. 4, pp. 561–580, 1992.

- [29] C. R. Vogel, "Non-convergence of the l-curve regularization parameter selection method," *Inverse Probl.*, vol. 12, no. 4, p. 535, 1996.
- [30] G. H. Golub, M. Heath, and G. Wahba, "Generalized cross-validation as a method for choosing a good ridge parameter," *Technometrics*, vol. 21, no. 2, pp. 215–223, 1979.
- [31] S. J. Reeves, "Optimal space-varying regularization in iterative image restoration," *IEEE Trans. Image Process.*, vol. 3, no. 3, pp. 319–324, 1994.
- [32] C. M. Stein, "Estimation of the mean of a multivariate normal distribution," *Ann Stat.*, pp. 1135–1151, 1981.
- [33] D. Van De Ville and M. Kocher, "Nonlocal means with dimensionality reduction and sure-based parameter selection," *IEEE Trans. Image Process.*, vol. 20, no. 9, pp. 2683–2690, 2011.
- [34] Y. Song, D. Brie, E.-H. Djermoune, and S. Henrot, "Regularization parameter estimation for non-negative hyperspectral image deconvolution," *IEEE Trans. Image Process.*, vol. 25, no. 11, pp. 5316–5330, 2016.
- [35] X. Wang, J. Chen, Q. Wei, and C. Richard, "Hyperspectral image super-resolution via deep prior regularization with parameter estimation," *IEEE Trans. Circuits Syst. Video Technol.*, 2021.
- [36] M. S. Almeida and M. A. Figueiredo, "Parameter estimation for blind and non-blind deblurring using residual whiteness measures," *IEEE Trans. Image Process.*, vol. 22, no. 7, pp. 2751–2763, 2013.
- [37] A. Lanza, M. Pragliola, and F. Sgallari, "Residual whiteness principle for parameter-free image restoration," *Electron. Trans. Numer. Anal.*, vol. 53, pp. 329–352, 2020.
- [38] A. Lanza, S. Morigi, F. Sciacchitano, and F. Sgallari, "Whiteness constraints in a unified variational framework for image restoration," *J. Math Imaging. Vis.*, vol. 60, no. 9, pp. 1503–1526, 2018.
- [39] W. Liu and J. Lee, "A 3-d atrous convolution neural network for hyperspectral image denoising," *IEEE Trans. Geosci. Remote Sens.*, vol. 57, no. 8, pp. 5701–5715, 2019.
- [40] K. Zhang, W. Zuo, Y. Chen, D. Meng, and L. Zhang, "Beyond a gaussian denoiser: Residual learning of deep cnn for image denoising," *IEEE Trans. Image Process.*, vol. 26, no. 7, pp. 3142–3155, 2017.
- [41] H. Zhao, O. Gallo, I. Frosio, and J. Kautz, "Loss functions for image restoration with neural networks," *IEEE Trans. Comput. Imaging*, vol. 3, no. 1, pp. 47–57, 2016.
- [42] F. Yasuma, T. Mitsunaga, D. Iso, and S. K. Nayar, "Generalized assorted pixel camera: postcapture control of resolution, dynamic range, and spectrum," *IEEE Trans. Image Process.*, vol. 19, no. 9, pp. 2241–2253, 2010.
- [43] N. Yokoya and A. Iwasaki, "Airborne hyperspectral data over chikusei," Space Application Laboratory, University of Tokyo, Japan, Tech. Rep. SAL-2016-05-27, May 2016.
- [44] A. Levin, Y. Weiss, F. Durand, and W. T. Freeman, "Understanding and evaluating blind deconvolution algorithms," in *Proc. IEEE Conf. Comput. Vis. Pattern Recognit. (CVPR)*, 2009, pp. 1964–1971.
- [45] D. P. Kingma and J. Ba, "Adam: A method for stochastic optimization," *arXiv preprint arXiv:1412.6980*, 2014.
- [46] K. He, X. Zhang, S. Ren, and J. Sun, "Delving deep into rectifiers: Surpassing human-level performance on imagenet classification," in *Proc. IEEE Int. Conf. Comput. Vis. (ICCV)*, 2015, pp. 1026–1034.
- [47] Z. Wang, A. C. Bovik, H. R. Sheikh, E. P. Simoncelli *et al.*, "Image quality assessment: from error visibility to structural similarity," *IEEE Trans. Image Process.*, vol. 13, no. 4, pp. 600–612, 2004.
- [48] L. Wald, "Quality of high resolution synthesised images: Is there a simple criterion?" in *Proc. 3rd conf. "Fusion of Earth Data"*. SEE/URISCA, 2000, pp. 99–103.
- [49] D. Krishnan and R. Fergus, "Fast image deconvolution using hyper-laplacian priors," in *Proc. Neural. Inf. Process. Systems. (NIPS)*, 2009, pp. 1033–1041.
- [50] L. Guo, X.-L. Zhao, X.-M. Gu, Y.-L. Zhao, Y.-B. Zheng, and T.-Z. Huang, "Three-dimensional fractional total variation regularized tensor optimized model for image deblurring," *Appl. Math. Comput.*, vol. 404, p. 126224, 2021.
- [51] S. Sreehari, S. V. Venkatakrishnan, B. Wohlberg, G. T. Buzzard, L. F. Drummy, J. P. Simmons, and C. A. Bouman, "Plug-and-play priors for bright field electron tomography and sparse interpolation," *IEEE Trans. Comput. Imaging*, vol. 2, no. 4, pp. 408–423, 2016.
- [52] A. M. Teodoro, J. M. Bioucas-Dias, and M. A. Figueiredo, "Scene-adapted plug-and-play algorithm with convergence guarantees," in *Proc. IEEE Int. Workshop. Mach. Learn. Signal Process. (MLSP)*. IEEE, 2017, pp. 1–6.
- [53] M. Zhao, J. Chen, and Z. He, "A laboratory-created dataset with ground truth for hyperspectral unmixing evaluation," *IEEE J. Sel. Top. Appl. Earth Observat. Remote Sens.*, vol. 12, no. 7, pp. 2170–2183, 2019.
- [54] M. Simões, J. Bioucas-Dias, L. B. Almeida, and J. Chanussot, "A convex formulation for hyperspectral image superresolution via subspace-based regularization," *IEEE Trans. Geosci. Remote Sens.*, vol. 53, no. 6, pp. 3373–3388, 2015.
- [55] R. E. Roger and J. F. Arnold, "Reliably estimating the noise in AVIRIS hyperspectral images," *Int. J. Remote Sens.*, vol. 17, no. 10, pp. 1951–1962, 1996.
- [56] D. Krishnan, T. Tay, and R. Fergus, "Blind deconvolution using a normalized sparsity measure," in *Proc. IEEE Conf. Comput. Vis. Pattern Recognit. (CVPR)*. IEEE, 2011, pp. 233–240.